



Contents lists available at SciVerse ScienceDirect

Journal of Controlled Release

journal homepage: www.elsevier.com/locate/jconrel

Rapid tumoritropic accumulation of systemically injected plateloid particles and their biodistribution

Anne L. van de Ven^{a,*}, Pilhan Kim^{b,g}, O'Hara Haley^b, Jean R. Fakhoury^a, Giulia Adriani^{a,c}, Jeffrey Schmulen^a, Padraig Moloney^d, Fazle Hussain^e, Mauro Ferrari^{a,1}, Xuewu Liu^{a,1}, Seok-Hyun Yun^{b,g,1}, Paolo Decuzzi^{a,f,**,1}

^a Department of Translational Imaging and Department of Nanomedicine, The Methodist Hospital Research Institute, 6670 Bertner Ave, Houston, TX 77030, USA

^b Wellman Center for Photomedicine and Harvard Medical School, Massachusetts General Hospital, 40 Blossom Street, Boston, MA 02114, USA

^c Department of Mechanical and Management Engineering, Politecnico di Bari, Via Re David 200, Bari 70125, Italy

^d Department of Mechanical Engineering and Materials Science, Rice University, 6100 Main St, Houston, TX 77005, USA

^e Department of Mechanical Engineering, University of Houston, Houston, TX 77204-4006, USA

^f Department of Experimental and Clinical Medicine, University of Magna Graecia, Catanzaro, 88100, Italy

^g Graduate School of Nano Science and Technology, KAIST, Daejeon, South Korea

ARTICLE INFO

Article history:

Received 19 August 2011

Accepted 19 October 2011

Available online 26 October 2011

Keywords:

Nanoparticles
Size and shape
Biodistribution
Tumor accumulation
Rational design
Intravital microscopy

ABSTRACT

Nanoparticles for cancer therapy and imaging are designed to accumulate in the diseased tissue by exploiting the Enhanced Permeability and Retention (EPR) effect. This limits their size to about 100 nm. Here, using intravital microscopy and elemental analysis, we compare the *in vivo* localization of particles with different geometries and demonstrate that plateloid particles preferentially accumulate within the tumor vasculature at unprecedented levels, independent of the EPR effect. In melanoma-bearing mice, 1000 × 400 nm plateloid particles adhered to the tumor vasculature at about 5% and 10% of the injected dose per gram organ (ID/g) for untargeted and RGD-targeted particles respectively, and exhibited the highest tumor-to-liver accumulation ratios (0.22 and 0.35). Smaller and larger plateloid particles, as well as cylindroid particles, were more extensively sequestered by the liver, spleen, and lungs. Plateloid particles appeared well-suited for taking advantage of hydrodynamic forces and interfacial interactions required for efficient tumoritropic accumulation, even without using specific targeting ligands.

© 2011 Elsevier B.V. All rights reserved.

1. Introduction

Many classes of nanoparticles (NPs) have been developed for diverse applications and some have shown potential in the treatment and imaging of diseases [1–4]. Drug encapsulation into NPs can provide significant improvements in pharmacokinetics, toxicity and biodistribution compared to freely administered molecules. Indeed, NP formulations of chemotherapeutic agents have increased by one to two orders of magnitude the peak drug accumulation in tumors [5], however, tumoritropic accumulation rarely exceeds 1% ID/g.

In cancer treatment and imaging, the commonly used strategy for maximizing NP accumulation relies on the enhanced permeation and retention (EPR) effect demonstrated by Maeda and collaborators 25 years ago [6,7]. The tumor vasculature is discontinuous with vessel

openings (fenestrations) whose size depends on the tumor type, stage and location [8–10]. Sufficiently small NPs (~100 nm) can passively exit the fenestrated vasculature and reach peak accumulation generally 12–24 h after injection. Curiously enough, major RES organs, such as the liver and spleen, are characterized by a fenestrated endothelium and utilize this same mechanism to sequester circulating foreign objects. Not surprisingly, a large portion of systemically injected agents and NPs end up accumulating in these RES organs.

Given the NP size limitation introduced by the EPR effect [9–13], efforts to enhance tumoritropic accumulation to-date have mostly focused on the chemical modification of the particle surface. Examples include steric stabilization to increase NP circulation time (*passive targeting*) [5,14], conjugation of ligands for cell-specific recognition (*active targeting*) [15–17], and active NP recruitment using endogenous [18–20] and exogenous [21,22] sources (*cooperative targeting*). Nevertheless, NP accumulation at the intended target is still lower than desired. A judicious choice of the size, shape, and surface combinations, unrelated to the EPR effect, would offer extra degrees of freedom for optimizing tumoritropic accumulation.

Blood presents brilliant examples of how different size, shape, and surface combinations can provide circulating objects with diverse

* Corresponding author. Tel.: +1 713 441 7449.

** Correspondence to: P. Decuzzi, Department of Translational Imaging and Department of Nanomedicine, The Methodist Hospital Research Institute, 6670 Bertner Ave, Houston, TX 77030, USA. Tel.: +1 713 441 7316.

E-mail addresses: avandeven@tmhs.org (A.L. van de Ven), pdecuzzi@tmhs.org (P. Decuzzi).

¹ These authors shared senior authorship.

functions. For instance, healthy red blood cells (RBCs) can continuously navigate the circulatory system for several weeks while delivering oxygen. The size, shape, and physiochemical properties of the RBC membrane allow these cells to avoid entrapment within the complex microvasculature and, in larger vessels, to repel from the endothelial walls and preferentially stay within the vessel center [23,24]. Conversely, platelets are mostly found in close proximity to the vessel walls, where they can periodically sense for and adhere to sites of vascular injury. This characteristic platelet behavior is ascribed to their small size ($3 \times$ smaller than RBCs) and quasi-discoidal shape [25,26].

Inspired by these phenomena, we reasoned that plateloid particles – thin disc-like particles – can be used for rapid, efficient, and specific accumulation within the tumor vasculature. Here, we fabricate nanoporous silicon particles with different geometries (size and shape) and surface properties; we monitor in real-time their dynamics using intravital microscopy and quantify, independently, their tissue accumulation by elemental analysis; and we interpret the *in vivo* data, using *in silico* mathematical modeling and *in vitro* adhesion assays, to elucidate the fine mechanisms regulating tumoritropic and RES accumulation.

2. Materials and methods

2.1. Animal models

Transgenic Tie2-GFP mice, engineered to express GFP in endothelial cells, were purchased from Jackson Labs (Bar Harbor, ME). The abdominal organs were exposed for intravital imaging via a 1.0 cm midline incision in the abdomen or flank. Melanoma tumors were generated in wild-type C57BL/6J mice (Charles River Laboratories, Wilmington, MA) by a one-time subcutaneous injection of 10^6 mouse B16 cells (ATCC, Manassas, VA). When tumors reached 3–5 mm in diameter, they were prepared for intravital imaging using a skin-flap procedure. Mice received a one-time injection of fluorescently labeled autologous red blood cells (RBCs) 1–3 days prior to imaging, in order to allow visualization of blood flow dynamics. Briefly, blood collected retro-orbitally was stained with lipophilic carbocyanine DiD (Invitrogen, Carlsbad, CA) at 37 °C using the manufacturer's recommended protocol and immediately re-injected behind the contra-lateral eye. Approximately 5% of the total RBCs were labeled per mouse. Thirty minutes after particle injection, mice were sacrificed by gravity perfusion with saline followed by 10% neutral buffered formalin. All intravital animal protocols were reviewed and approved by the IACUC at Massachusetts General Hospital.

2.2. Intravital image acquisition and analysis

Organ-specific accumulation of plateloid silicon particles *in vivo* was monitored in real-time using a custom, video-rate laser scanning confocal microscope equipped with an x-axis polygon scanner, y-axis galvanometer, 3 lasers (491, 532, and 635 nm), and 3 photomultiplier tubes [34,35] (Supplementary Information). Band pass filters of 30–35 nm width were centered at 425 nm (GFP), 579 nm (particles), and 670 nm (red blood cells). Anesthetized, surgically opened mice were positioned upon the heated stage and injected retro-orbitally with 5×10^8 particles of a single size (in 50 μ l PBS). Three-channel images were acquired from a single organ per animal at 30 frames per second from the time of injection using a 40×0.6 NA dry objective with a pinhole of 100 μ m. To minimize local phototoxicity and compensate for tissue heterogeneity, randomly selected non-overlapping regions of interest (ROI, $250 \times 250 \times 6 \mu$ m) were imaged continuously for 3 min before moving to the next ROI. Animals were imaged for 30 min and then sacrificed as described above. A total of 4–8 organs/particle/strain were imaged in real-time. To determine particle accumulation as a function of time, the number of particles per field of view (FOV) was estimated from video stills at 10-second intervals using ImageJ v1.34 (NIH, Bethesda, MD). The 8-bit images were split by color, single pixel noise was removed using a minimum noise filter, and then the

total number pixels above a threshold intensity of 50 was divided by the average number pixels per particle. The average number of pixels per particle was experimentally determined for each particle size and confirmed by comparing manual particle counts to automated particle counts. The number of particles per FOV was divided by the optical imaging volume and plotted as a function of time. Representative raw IVM images and quantitative data is shown in Supplementary Fig. 9.

2.3. Particle fabrication and conjugation

Porous silicon particles were fabricated by modification of previously described protocols [33], as detailed in the Supplementary Information. Images (Supplementary Fig. 8) and characterization data (Supplementary Table 1) are also provided.

2.4. The probability of particle adhesion to the vascular walls

At time $t = 0$, the particle is in close proximity of the vessel wall with all potential ligand–receptor bonds still open (no adhesion). With time, ligands and receptors interact and tend to form molecular bonds with a probability $p_n(t)$ of having n bonds close at time t governed by the equation [52]

$$\frac{dp_n}{dt} = [A_c m_r - (n-1)][A_c m_l - (n-1)] \frac{k_f^{(n)}(t)}{A_c} p_{n-1}(t) + (n+1)k_r^{(n+1)}(t) p_{n+1}(t) - \left[(A_c m_r - n)(A_c m_l - n) \frac{k_f^{(n+1)}(t)}{A_c} + n k_r^{(n)}(t) \right] p_n(t) \quad (1)$$

where $k_f^{(n)}(t)$ and $k_r^{(n)}(t)$ are the forward (association) and reverse (dissociation) rates at time t for n close bonds. A_c is the area of adhesion which is given by πd^2 for a plateloid particle with diameter d . Assuming for simplicity a uniform distribution of the hydrodynamic dislodging forces over the n molecular bonds at each time t , the reactions rates take the explicit forms

$$k_r^{(n)}(t) = k_{r0} \exp \left[\frac{\chi F_{tot}(t)}{k_B T m_b A_c} \right] \quad (2)$$

$$k_f^{(n)}(t) = k_{f0} \left[1 + \frac{\chi F_{tot}(t)}{k_B T m_b A_c} \right]^{-1}$$

where χ ($= 0.1$ nm) is the characteristic bond length, and $k_B T$ is the Boltzmann thermal energy ($= 4.14 \times 10^{-21}$ J). k_{f0} and k_{r0} are the forward and reverse rates at zero mechanical load, and their ratio k_{a0} ($= k_{f0}/k_{r0}$) is the ligand–receptor affinity at zero mechanical load. The ligand–receptor bond density m_b is equal to the minimum value between m_r and m_l . Eq. (2) is then solved numerically for different values of n imposing the initial conditions ($p_n(0) = 0$ for $n > 1$; and $p_0(0) = 1$) and the closure condition ($\sum_{i=0}^{m_r A_c} p_n(t) = 1$ at each time t). The probability of adhesion P_a is defined as the probability of having at least one ligand–receptor bond close and is easily estimated as $P_a(t) = 1 - p_0(t)$.

The generalized force F exerted over the adhering plateloid particle are estimated, following previous work [53], as $F = \pi A \mu S a^2$, where S is the wall shear rate, μ is the plasma viscosity (2.5×10^{-3} Pa \times s), and the coefficient A depends on the aspect ratio b/a , which is ~ 0.35 in the present analysis.

3. Results and discussion

3.1. Nanoporous silicon plateloids and cylindroids

Precise control over multiple scales of the NP size, shape, and surface properties is reliably achieved with few technologies [27–30]. Nanoporous silicon particles were chosen for these studies due to their documented advantages in the treatment and imaging of tumors

[31–35]. Particles of different geometries were fabricated using two consecutive steps: formation of a porous silicon film and micropatterning. The particle porosity and pore size were tailored by electrochemical etching, controlling parameters such as silicon doping, etching current, and HF concentration; while the particle size was precisely defined by photolithography. Since the pore structure and particle geometry are independently controlled, a wide range of size, shape and pore morphologies can be reliably achieved with such an approach [36]. Three sizes of plateloid particles with similar aspect ratios were fabricated: 600×200 nm, 1000×400 nm, and 1800×600 nm. Two sizes of cylindroid particles were fabricated: 1500×200 nm and 1800×400 nm, which exhibit a volume equivalent to that of the two smaller plateloid particles. Fig. 1a shows SEM images of plateloid and cylindroid particles before and after release from the original silicon wafer.

Particles of plateloid and cylindroid shape are expected to exhibit fairly complex dynamics under flow and will tend to drift laterally across the stream lines in a periodic manner (Fig. 1b – Margination inset). Particle interaction with the vessel walls is a critical step for the recognition of the diseased vasculature. *In silico* mathematical models have shown that lateral drifting diminishes as the NP size decreases, becoming irrelevant for particles of ~ 100 nm or less [37]. Also, moving from spherical to anisometric particles increases lateral drifting, as well as the probability of firm vascular adhesion because of the larger surface area exposed to the endothelial wall [38] (Fig. 1b – Adhesion inset). Sub-micrometer and micrometer anisometric particles offer the further advantage of a high cargo capacity, allowing for the localized release of therapeutic and imaging agents at the site of vascular adhesion (Fig. 1b – Release inset).

The nanoporous silicon particles were labeled with fluorescent dye molecules for optical tracking within the blood flow. Their dynamics was monitored in live mice following systemic injection using high-resolution, video-rate intravital microscopy (IVM) [39,40]. Fig. 1c captures some of the distinctive features exhibited by individual particles within the microvasculature, including differential transport velocities and adhesion to the vessel walls.

3.2. Particle localization at the organ scale

To evaluate the importance of particle geometry (size and shape) for organ accumulation, the biodistribution of individual particles was examined (Fig. 2). Fig. 2a shows representative images of particle accumulation in different organs, collected *in vivo* 1 h after injection. Videos of particle accumulation and additional images are provided in the supplementary information (Supplementary Figs. S1 and S2, and Supplementary Movies 1 and 2). This IVM technique was used, for the first time, to quantify the time-dependent accumulation of the particles in live mice (Fig. 2a). Fig. 2b shows the accumulation of 600×200 nm and 1000×400 nm plateloid particles in three different organs of wild-type, melanoma-bearing mice. Unlike EPR-based delivery strategies, the accumulation of these particles was most rapid for the first 5–10 min after injection, and then began to level off. Note that, in the liver and spleen, 600×200 nm plateloid particles accumulated faster and in greater numbers ($\sim 3 \times$) than the 1000×400 nm. This trend was reversed in tumor tissue ($\sim 1/4 \times$). The cumulative particle uptake measured by IVM is shown in Fig. 3a, where the effect of particle geometry can be readily appreciated.

Using ICP-AES, the total number of accumulated particles was independently quantified in whole organs after animal sacrifice. The particle biodistribution, expressed in terms of percentage of the injected dose normalized by the organ weight, shows that geometry (size and shape) plays a significant role in the ability of NPs to preferentially accumulate in different tissues (Fig. 3b). In liver and spleen, 600×200 nm plateloid particles display the highest accumulation efficiency. In contrast, cylindroid particles accumulate at much higher levels than plateloid particles in the lungs. Most interestingly, in the

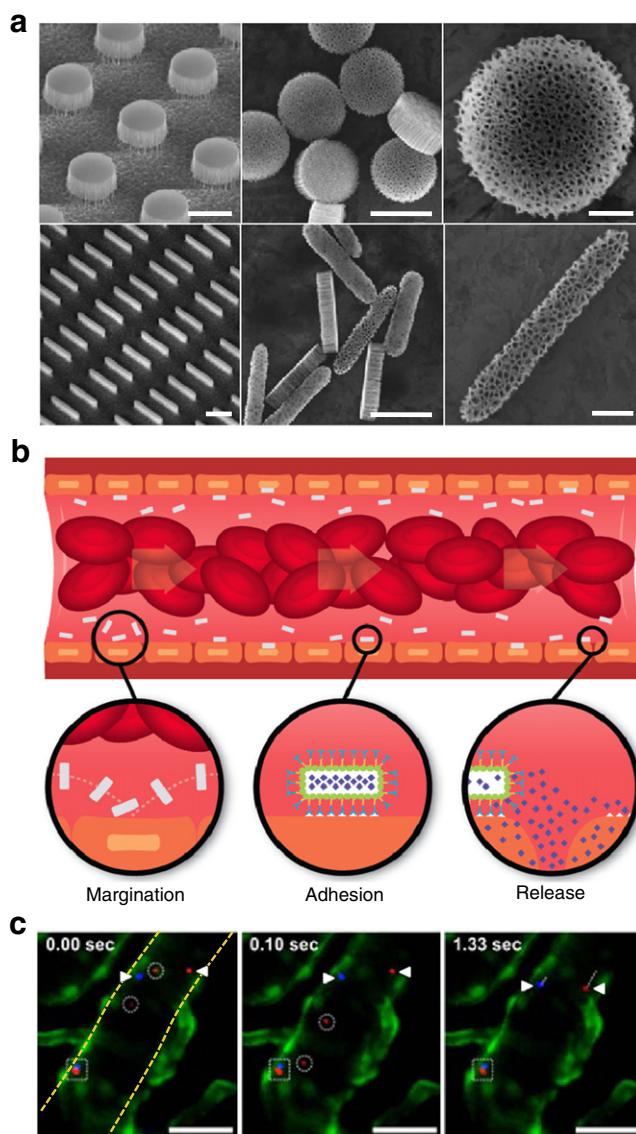


Fig. 1. Rationally designed nanoporous silicon particles. a, SEM images of nanoporous plateloid (1000×400 nm) and cylindroid (1500×200 nm) silicon particles micropatterned from a porous film before (left) and after release (middle, right) (scale bars, 1.0, 1.0, and 0.25 μm). b, Longitudinal cross-section illustration of a blood vessel containing circulating red blood cells and silicon particles traveling through and adhering to the walls. Margination inset: The lateral drifting of anisometric particles promotes periodic interaction with the vessel walls; Adhesion inset: The large surface area of anisometric particles favors specific and non-specific interactions with receptors on the endothelial surface; Release inset: The release of cargo by adherent particles facilitates localized delivery into the underlying tissue. c, Intravital microscopy images showing time-dependent trajectories of individual 600×200 nm (red) and 1000×400 nm (blue) plateloid silicon particles in the ear venule of a Tie-2 GFP mouse. The triangles indicate relatively slow moving particles ($\mu\text{m/s}$), the circles indicate fast moving particles ($\mu\text{m/ms}$), and the square indicates particles adhered to the vessel wall. Endothelial cells are colored green, vessel walls are demarcated in yellow (scale bar, 50 μm).

tumor, 1000×400 nm plateloid particles demonstrate the highest accumulation efficiency of all particles examined (5% ID/g tumor). The trends observed in the IVM data (Fig. 3a) and ICP-AES data (Fig. 3b, Supplementary Fig. 3) are in good qualitative agreement.

Several of the animals receiving cylindroid particles died spontaneously between 30 and 60 min after injection, showing signs of labored breathing before death and gross signs of lung emboli upon necropsy. It is possible that these rigid cylindroid particles have a similar capacity for causing lung emboli as the so called 'ugly' nanotubes

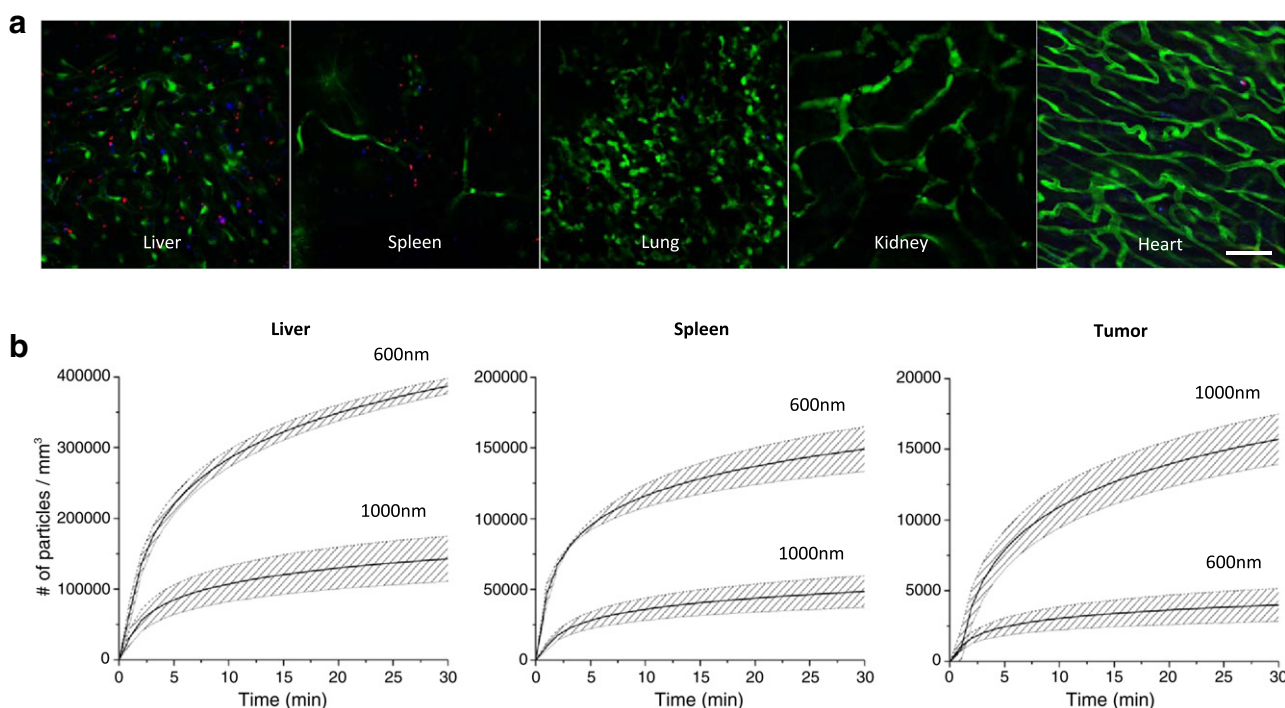


Fig. 2. Biodistribution of plateloid particles in live mice. a, Distribution of 600 × 200 nm (red) and 1000 × 400 nm (blue) plateloid silicon particles in different organs of Tie2-GFP mice 1 h after simultaneous systemic injection (scale bar, 50 μm). b, Time-dependent accumulation of plateloid particles (injected independently) in two major RES organs – the liver and the spleen – and in the tumor tissue of melanoma-bearing mice, measured using intravital microscopy. Data is plotted as a mean curve ± 1 SD (n = 4 animals).

[41]. Shorter cylindroid particles may provide different biodistributions, but also much lower payloads due to their smaller volume. Since no complications were observed with plateloid particles, these were used for assessing the importance of molecular targeting in tumors.

Fluorescently tagged plateloid particles were derivatized with a cyclic arginine–glycine–asparagine (RGD-4 C) peptide via a short PEG linker to produce particles of identical size, shape, and surface charge

but with a high affinity for the $\alpha_v\beta_3$ integrins overexpressed on the tumor endothelium. Fig. 4a shows the time-dependent accumulation of targeted and untargeted plateloid particles in tumors, measured with IVM. The cumulative particle uptake was independently quantified using ICP-AES (Fig. 4b). For untargeted particles, the level of accumulation varied from 1.2% (600 × 200 nm) to 5.1% (1000 × 400 nm) to 3.2% ID/g (1800 × 600 nm). The use of RGD-4 C moieties increases tumor-specific accumulation, presenting as 4.5% (600 × 200 nm), 8.1%

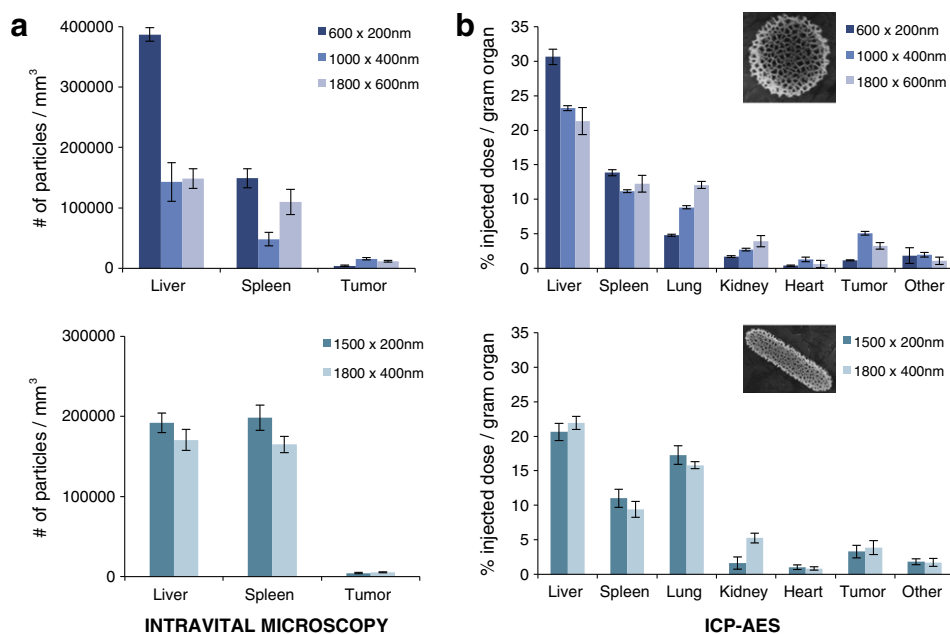


Fig. 3. Cumulative particle localization at the organ level: The effect of particle geometry. a, Intravital data on the cumulative uptake of plateloid (top) and cylindroid (bottom) particles 30 minutes after injection. b, ICP-AES data on the cumulative uptake of plateloid (top) and cylindroid (bottom) particles expressed as a percentage of the injected dose normalized by the tissue mass. Similar trends are observed with the two independent techniques.

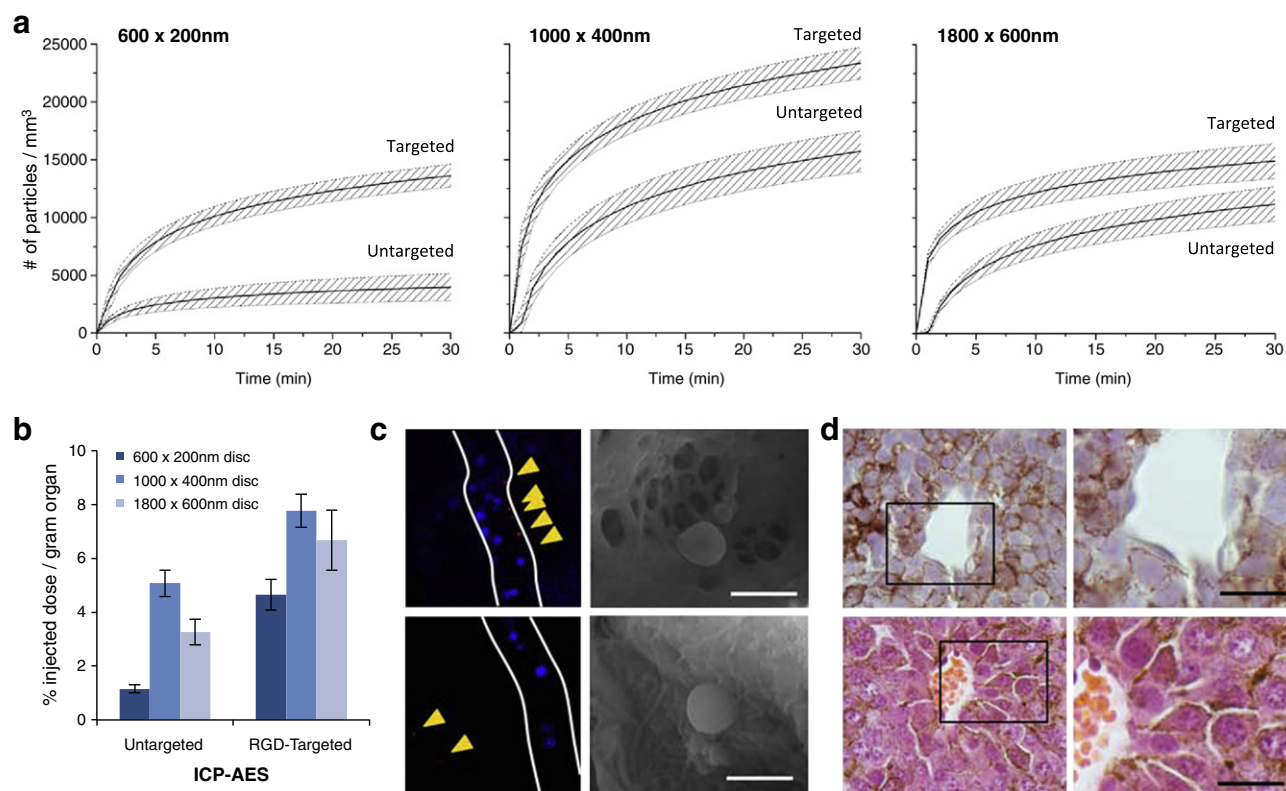


Fig. 4. Accumulation of untargeted and RGD-targeted platelet particles in melanoma tumors. a, Intravital microscopy data on the time-dependent accumulation of 600×200 nm (left), 1000×400 nm (center), and 1800×600 nm (right) platelet particles. b, ICP-AES data on the cumulative particle uptake expressed as percentage of the injected dose normalized by the tumor mass. c, Stills extracted from intravital videos reveal that 1000×400 nm particles accumulate within the tumor vasculature (top left), whereas some 600×200 nm particles extravasate out of the vasculature (bottom left). The SEM sections clearly show the fenestrations in the tumor vasculature and their size relative to the platelet particles (scale bar, $1.0 \mu\text{m}$). d, Representative histological images of the tissue surrounding the tumor vasculature. The vessel wall is poorly organized with gaps between endothelial cells (top). The tumor cells are poorly packed, resulting in gaps between cells (bottom) (scale bar, $1.0 \mu\text{m}$).

(1000×400 nm), and 6.5% ID/g (1800×600 nm) respectively. Interestingly, a maximum appears for the 1000×400 nm particles, regardless of the surface properties. The enhancement in particle accumulation with RGD-4 C addition was size-dependent, with the smallest particles showing the greatest enhancement (300% versus 50% for 600×200 and 1000×400 nm particles respectively). The 1000×400 nm particles exhibit the highest tumor-to-liver accumulation ratio, being equal to about 0.22 and 0.35 for untargeted and targeted platelets respectively. This unprecedented, rapid tumorigenic accumulation was achieved using particles significantly larger than known tumor fenestration sizes.

3.3. Particle localization at the sub-organ scale

In tumors, the 1000×400 nm particles were observed to be confined within the blood vessels using both IVM and SEM imaging (Fig. 4c, top). Particle adhesion occurred in both fenestrated and non-fenestrated regions of the tumor vasculature (Supplementary Fig. 4). Differently, some 600×200 nm particles (5–10% untargeted, <1% targeted) were seen outside the vascular compartment (Fig. 4c, bottom). This is likely associated with the highly fenestrated vessels and poorly organized melanoma tissue through which the smaller platelet particles may diffuse (Fig. 4d).

For the major RES organs, particle association with cells of the immune system was studied using IVM, immunocytochemistry, and histological analysis (Fig. 5 and Supplementary Figs. 5 and 6). Immunocytochemistry images showed that >80% of platelet and cylindroid particles in the liver were associated with Kupffer cells (Fig. 5a,b and Supplementary Fig. 5). In the spleen, a similar trend was observed for the two larger platelet particles (>70%), whereas only 50% of the 600 nm particles associated with the splenic macrophages (Fig. 5a,b). This difference may be ascribed to the smaller size of the 600×200 nm particles, which are more prone to geometrical trapping in the splenic fenestrations, as confirmed by

histological analysis (Fig. 5c). Like the 600×200 nm platelet particles, the 1500×200 nm cylindroid particles displayed an increased propensity to accumulate at the margins of the white pulp, as compared to their thicker counterparts which remained uniformly distributed in the red pulp (Supplementary Fig. 5b). Fig. 5d,e shows SEM sections of the liver vasculature capturing different stages of the cell–particle interaction *in vivo*: first circulating particles firmly adhere to the surface of Kupffer cells (Fig. 5d), then pseudopodia protrude out of the cell membrane and start to gently embrace the particles (Fig. 5d), and eventually particles are pulled inside the cell (Fig. 5e). In the tumor and other tissues, the percentage of particles associated with macrophages is negligibly small (Fig. 5a, Supplementary Fig. 5a).

3.4. Mechanisms regulating preferential particle accumulation

Vascular adhesion and internalization by immune cells lining the vessel walls, such as the Kupffer cells in the liver and the splenic macrophages, are finely regulated by the interplay between hydrodynamic forces and interfacial interactions. The latter primarily originate from the binding of receptors, expressed over the cell membrane with a density m_r , to ligands, coating the particles surface with a density m_l [38]. Colloidal forces may also arise at the particle–cell interface but are generally much weaker than molecular interactions, especially in plasma [42]. Particle surfaces can be functionalized with ligands during synthesis or opsonized upon contact with the blood stream [43]. Nanoporous silicon particles are coated to different extents by plasma molecules which act as ligands for the CR1 and Fc receptors expressed by cells of the immune system [44].

Following the formulation presented in Section 2, a probability of particle adhesion P_a to the blood vessels can be estimated as a function of design parameters (geometry, ligand density m_l , ligand–receptor

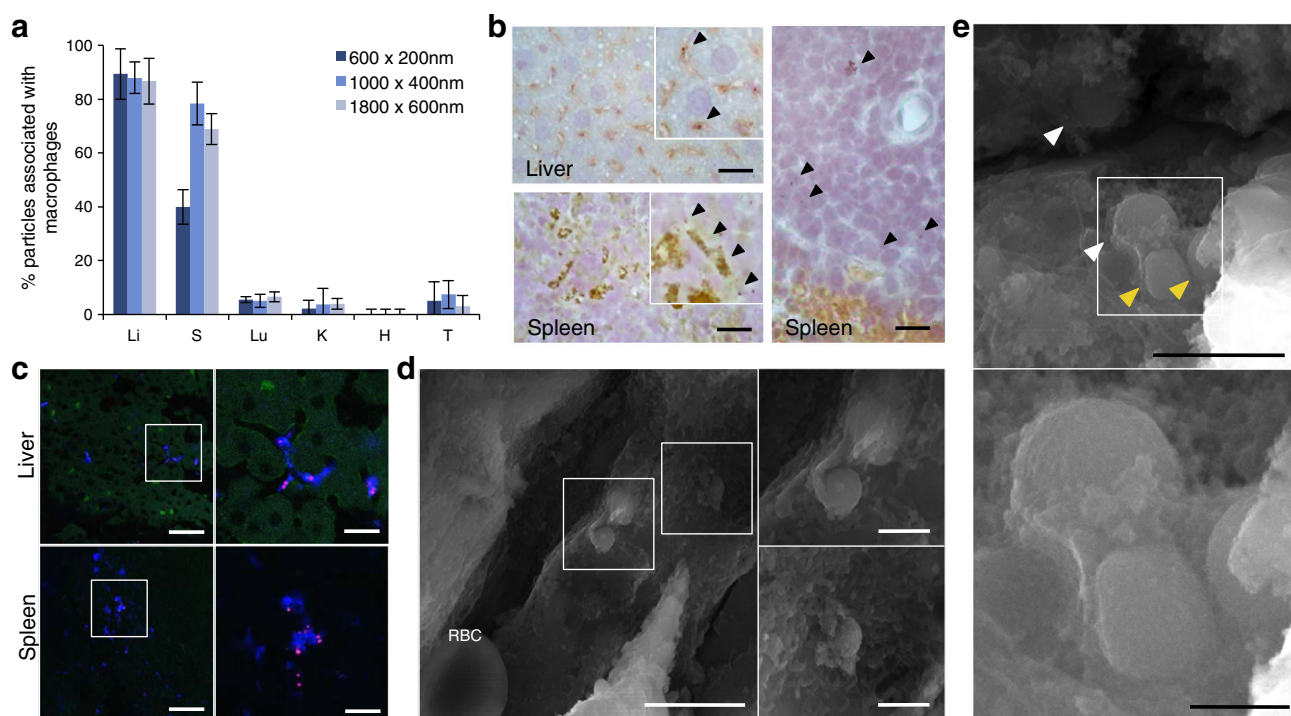


Fig. 5. Sequestration of plateloid particles by immune cells. a, Percentage of particles co-localized with immune cells in different organs, measured using immunocytochemistry of fixed tissue cross-sections (Li: Liver; S: Spleen; Lu: Lungs; K: Kidneys; H: Heart and T: Tumor). b, Confocal fluorescence images of 1000×400 nm particles (red) co-localizing with CD204+ macrophages (blue) in fixed liver and spleen tissue. c, IHC images of 1000×400 nm (left) and 600×200 nm (right) particles in the liver and spleen. CD204+ macrophages are stained in brown. d, SEM images of 1000×400 nm particles in the liver vasculature being internalized by a Kupffer cell. A red blood cell (RBC) is visible at the bottom left of the larger image (scale bars, 5.0 and 1.0 μm). e, SEM images of 600×200 nm particles in the liver vasculature. The white arrows indicate particles undergoing internalization (scale bars, 2.0 and 0.5 μm).

affinity k_a) and biophysical conditions at the adhesion site (wall shear rate S , receptor density m_r). Fig. 6a shows the variation of P_a for plateloid particles with a diameter d and for different values of the shear rate S , having fixed all the other parameters. For wall shear rates typically found in the leaky tumor vessels (low S) [8], the P_a curves exhibit a maximum at about 1000 nm. Moving from pathological to normal vessels ($S > 500 \text{ s}^{-1}$), the maximum in strength of adhesion occurs at smaller d (Supplementary Information). The existence of an optimal geometry (size and shape) maximizing vascular adhesion was previously conjectured [37] and explained as: for small particles, the interfacial area offered to the vessel walls for developing stable and strong adhesive forces is insufficient (*area limited regime*); on the other hand, for large particles, the hydrodynamic dislodging forces are excessively large to be balanced by interfacial adhesion interactions (*force limited regime*). This fine balance was recently observed experimentally for spherical beads [45] and, here, confirmed for plateloid particles (Fig. 6b).

Using an experimental parallel plate flow chamber apparatus, the adhesive strength of untargeted plateloid particles was quantified as a function of diameter d and wall shear rate S . As shown in Fig. 6b, the 1000 nm particles adhere more avidly at all S , followed by the 1800 nm and by the 600 nm particles. As S increases, the overall number of adhering particles reduces. The strong agreement between the tumor accumulation data (Fig. 4b), theoretical predictions (Fig. 6a), and *in vitro* experiments (Fig. 6b) suggests that vascular adhesion may be dominant mechanism for their tumor accumulation. This is also supported by the IVM images presented in Fig. 4c.

The effect of the receptor density m_r and ligand–receptor affinity k_a on the probability of adhesion P_a was also estimated and shown in Fig. 6c,d. Both parameters, although independent, characterize the specificity of molecular targeting. Consequently, the two plots in Fig. 6c,d are qualitatively similar and manifest the growth in adhesive strength with the improvement in molecular specificity (i.e. larger m_r ,

and k_a). Indeed, this is true under the idealized conditions of the *in silico* modeling and *in vitro* experiments, but it is also in agreement with the accumulation data presented for the RGD-4 C modified particles (Fig. 4b). Again, the optimal diameter d is not significantly affected by the particles surface properties (targeted and untargeted), unless extremely large m_r and k_a are considered (Supplementary Information).

Particles in the liver and the spleen, unlike tumors, are taken up by immune cells lining the blood vessels in these organs (Fig. 5). Therefore, adhesion and subsequent cell internalization should be considered in series to correctly interpret the quantitative data of Fig. 3. In this case, particle adhesion is mediated by the CR1 and Fc receptors, which are highly expressed on the membrane of phagocytic cells ($m_r = 10^3$ and $10^5 \text{ #}/\mu\text{m}^2$, depending on the stimulation state [46]). Under these conditions, P_a is extremely large regardless of the particle size. On the other hand, the internalization rate is affected by the particle size. In agreement with data in the literature [47], J774.1 macrophages were found *in vitro* to internalize 600×200 nm particles faster than the 1000×400 nm (Supplementary Fig. 7). As a consequence, the probability of internalization – probability of adhesion \times rate of internalization – is greater for 600×200 nm particles compared to larger particles. This would explain the higher accumulation observed for the smaller plateloid particles in the liver and spleen (Figs. 2a and 3).

4. Conclusions

In current practice, systemically injected NPs rely on the EPR effect to preferentially accumulate within tumors. Using this delivery strategy, few NPs have achieved tumor accumulation greater than 1% ID/g. Here we demonstrate rapid (<1 h) and unprecedented (~10% ID/g) accumulation of 1000×400 nm plateloid particles in the tumor vasculature. The use of an EPR-independent delivery strategy allowed additional degrees of freedom over traditional tumorotropic accumulation schemes.

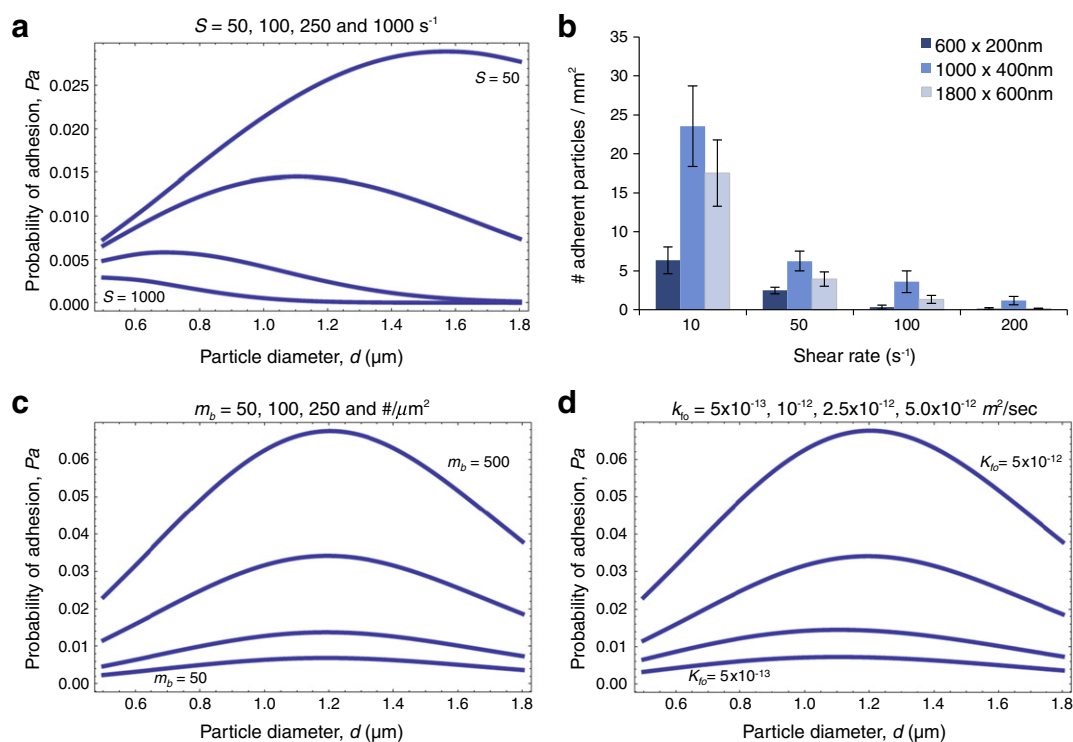


Fig. 6. Adhesion of platelet particles. a, The probability of adhesion (P_a) for platelet particles is shown as a function of the diameter d and for different shear rates S ($m_r = 10^{+2}$ #/ μm^2 ; $m_l = 10^{+4}$ #/ μm^2 ; $k_{ao} = 10^{-9}$ μm^2); b, Number of platelet particles adhering per unit area to the bottom of a parallel plate flow chamber, under different hydrodynamic conditions; c, P_a as a function of the particle diameter d and for different receptor densities m_b ($S = 100$ sec^{-1} ; $m_r = 10^{+2}$ #/ μm^2 ; $k_{ao} = 10^{-9}$ μm^2); d, P_a as a function of the diameter d and for different ligand-receptor affinities k_0 ($S = 100$ sec^{-1} ; $m_r = 10^{+2}$ #/ μm^2 ; $m_l = 10^{+4}$ #/ μm^2 ; $k_{ro} = 10^{-3}$ μm^2).

Particle size, shape, and surface properties were all found to play an important role. In particular, 1000×400 nm platelet particles appeared well-suited for taking advantage of hydrodynamic forces and interfacial interactions required for efficient tumor-tropic accumulation, even without the use of specific targeting ligands. Smaller platelet particles accumulated more extensively in the liver and spleen, whereas larger platelet particles deposited more in the lungs. Cylindroid particles exhibited a significantly lower tumor-to-liver accumulation ratio.

Platelet particles designed to recognize and adhere to diseased vessels may be employed to deliver anti-angiogenic agents directly to endothelial cells [48], thermally ablate blood vessels supplying the tumor mass [49], or to locally deploy cargos (drug molecules, contrast agents, NPs, etc.) to tumors characterized by small fenestrations. Furthermore, they may exploit the huge diversity of biomarkers that differentiate normal from abnormal endothelia for potentially treating and imaging a variety of pathologies, including cardiovascular, hemorrhagic, and neurodegenerative diseases [50,51].

Collectively, these results demonstrate that platelet particles of the proper size, shape, and surface properties significantly enhance tumor-tropic particle accumulation. Without relying on the EPR effect, they may offer notable therapeutic and imaging potential for a variety of diseases.

Supplementary materials related to this article can be found online at doi:10.1016/j.jconrel.2011.10.021.

Acknowledgments

This work was supported by Telemedicine and Advanced Technology Research Center (TATRC)–United States Army Medical Research Acquisition Activity (USAMRAA) through the pre-centre grant W81XWH-09-2-0139 of the Alliance for Nano Health. This work was also partially supported through grants from the National Institutes of Health (USA)

(NIH)U54CA143837 and U54CA151668, and the Department of Defense (DoD) grant W81XWH-09-1-0212. The authors would like to thank Mr. Matthew Landry for helping with the graphical work, Mr. Aaron Mack for advice on particle conjugation and ICP-AES protocols, as well as Dr. W.M. Steve Lee and Dr. Jinwoo Choi for helping with animal preparations. PD would like to thank the President and staff at the University of Magna Graecia-Italy for their support.

References

- [1] T.M. Allen, P.R. Cullis, Drug delivery systems: entering the mainstream, *Science* 19 (2004) 1818–1822.
- [2] H.C. Huang, S. Barua, G. Sharma, S.K. Dey, K. Rege, Inorganic nanoparticles for cancer imaging and therapy, *J. Control. Release* 155 (2011) 344–357.
- [3] M. Ferrari, Cancer nanotechnology: opportunities and challenges, *Nat. Rev. Cancer* 5 (2005) 161–171.
- [4] D. Peer, J.M. Karp, S. Hong, O.C. Farokhzad, R. Margalit, R. Langer, Nanocarriers as an emerging platform for cancer therapy, *Nat. Nanotechnol.* 2 (2007) 751–760.
- [5] D.C. Drummond, O. Meyer, K. Hong, D.B. Kirpotin, D. Papahadjopoulos, Optimizing liposomes for delivery of chemotherapeutic agents to solid tumors, *Pharmacol. Rev.* 51 (1999) 691–743.
- [6] Y. Matsumura, H. Maeda, A new concept for macromolecular therapeutics in cancer chemotherapy: mechanism of tumor-tropic accumulation of proteins and the antitumor agent smancs, *Cancer Res.* 46 (1986) 6387–6392.
- [7] H. Maeda, J. Wu, T. Sawa, Y. Matsumura, K. Hori, Tumor vascular permeability and the EPR effect in macromolecular therapeutics: a review, *J. Control. Release* 65 (2000) 271–284.
- [8] R.K. Jain, T. Stylianopoulos, Delivering nanomedicine to solid tumors, *Nat. Rev. Clin. Oncol.* 7 (2010) 653–664.
- [9] F. Yuan, M. Leunig, S.K. Huang, D.A. Berk, D. Papahadjopoulos, R.K. Jain, Microvascular permeability and interstitial penetration of sterically stabilized (stealth) liposomes in a human tumor xenograft, *Cancer Res.* 54 (1994) 3352–3356.
- [10] S.K. Hobbs, W.L. Monsky, F. Yuan, W.G. Roberts, L. Griffith, V.P. Torchilin, R.K. Jain, Regulation of transport pathways in tumor vessels: role of tumor type and micro-environment, *Proc. Natl. Acad. Sci. U. S. A.* 95 (1998) 4607–4612.
- [11] R.B. Campbell, D. Fukumura, E.B. Brown, L.M. Mazzola, Y. Izumi, R.K. Jain, V.P. Torchilin, L.L. Munn, Cationic charge determines the distribution of liposomes between the vascular and extravascular compartments of tumors, *Cancer Res.* 62 (2002) 6831–6836.

- [12] M. Dellian, F. Yuan, S. Trubetskoy, P. Torchilin, R.K. Jain, Vascular permeability in a human tumour xenograft: molecular charge dependence, *Br. J. Cancer* 82 (2000) 1513–1518.
- [13] M. Stroh, J.P. Zimmer, D.G. Duda, T.S. Levchenko, K.S. Cohen, E.B. Brown, D.T. Scadden, V.P. Torchilin, M.G. Bawendi, D. Fukumura, R.K. Jain, Quantum dots spectrally distinguish multiple species within the tumor milieu *in vivo*, *Nat. Med.* 11 (2005) 678–682.
- [14] S.M. Moghimi, A.C. Hunter, J.C. Murray, Nanomedicine: current status and future prospects, *FASEB J.* 19 (2005) 311–330.
- [15] T.A. Elbayoumi, V.P. Torchilin, Enhanced accumulation of long-circulating liposomes modified with the nucleosome-specific monoclonal antibody 2C5 in various tumours in mice: gamma-imaging studies, *Eur. J. Nucl. Med. Mol. Imaging* 33 (2006) 1196–1205.
- [16] J. Cheng, B.A. Teply, I. Sherif, J. Sung, G. Luther, F.X. Gu, E. Levy-Nissenbaum, A.F. Radovic-Moreno, R. Langer, O.C. Farokhzad, Formulation of functionalized PLGA-PEG nanoparticles for *in vivo* targeted drug delivery, *Biomaterials* 28 (2007) 869–876.
- [17] M.D. Wang, D.M. Shin, J.W. Simons, S. Nie, Nanotechnology for targeted cancer therapy, *Expert. Rev. Anticancer. Ther.* 7 (2007) 833–837.
- [18] W. Lu, C. Xiong, G. Zhang, Q. Huang, R. Zhang, J.Z. Zhang, C. Li, Targeted photothermal ablation of murine melanomas with melanocyte-stimulating hormone analog-conjugated hollow gold nanospheres, *Clin. Cancer Res.* 15 (2009) 876–886.
- [19] J.H. Park, G. von Maltzahn, M.J. Xu, V. Fogal, V.R. Kotamraju, E. Ruoslahti, S.N. Bhatia, M.J. Sailor, Cooperative nanomaterial system to sensitize, target, and treat tumors, *Proc. Natl. Acad. Sci. U. S. A.* 107 (2010) 981–986.
- [20] G. von Maltzahn, J.H. Park, K.Y. Lin, N. Singh, C. Schwöppe, R. Mesters, W.E. Berdel, E. Ruoslahti, M.J. Sailor, S.N. Bhatia, Nanoparticles that communicate *in vivo* to amplify tumour targeting, *Nat. Mater.* 10 (2011) 545–552.
- [21] B. Chertok, A.E. David, Y. Huang, V.C. Yang, Glioma selectivity of magnetically targeted nanoparticles: a role of abnormal tumor hydrodynamics, *J. Control. Release.* 122 (2007) 315–323.
- [22] H.L. Liu, M.Y. Hua, H.W. Yang, C.Y. Huang, P.C. Chu, J.S. Wu, I.C. Tseng, J.J. Wang, T.C. Yen, P.Y. Chen, K.C. Wei, Magnetic resonance monitoring of focused ultrasound/magnetic nanoparticle targeting delivery of therapeutic agents to the brain, *Proc. Natl. Acad. Sci. U. S. A.* 107 (2010) 15205–15210.
- [23] S. Kim, P.K. Ong, O. Yalcin, M. Intaglietta, P.C. Johnson, The cell-free layer in microvascular blood flow, *Biorheology* 46 (2009) 181–189.
- [24] H.H. Lipowsky, Microvascular rheology and hemodynamics, *Microcirculation* 12 (2005) 5–15.
- [25] C. Yeh, E.C. Eckstein, Transient lateral transport of platelet-sized particles in flowing blood suspensions, *Biophys. J.* 66 (1994) 1706–1716.
- [26] M. Saadatmand, T. Ishikawa, N. Matsuki, M. Jafar Abdekhodaie, Y. Imai, H. Ueno, T. Yamaguchi, Fluid particle diffusion through high-hematocrit blood flow within a capillary tube, *J. Biomech.* 44 (2011) 170–175.
- [27] M.H. Cohen, K. Melnik, A.A. Boiarski, M. Ferrari, F.J. Martin, Microfabrication of silicon-based nanoporous particulates for medical applications, *Biomed. Microdevices* 5 (2003) 253–259.
- [28] S.E. Gratton, P.D. Pohlhaus, J. Lee, J. Guo, M.J. Cho, J.M. Desimone, Nanofabricated particles for engineered drug therapies: a preliminary biodistribution study of PRINT nanoparticles, *J. Control. Release.* 21 (2007) 10–18.
- [29] J.A. Champion, Y.K. Katara, S. Mitragotri, Making polymeric micro- and nanoparticles of complex shapes, *Proc. Natl. Acad. Sci. U. S. A.* 104 (2007) 11901–11904.
- [30] G. Acharya, C.S. Shin, M. McDermott, H. Mishra, H. Park, I.C. Kwon, K. Park, The hydrogel template method for fabrication of homogeneous nano/microparticles, *J. Control. Release.* 141 (2010) 314–319.
- [31] E. Tasciotti, X. Liu, R. Bhavane, K. Plant, A.D. Leonard, B.K. Price, M.M. Cheng, P. Decuzzi, J.M. Tour, F. Robertson, M. Ferrari, Mesoporous silicon particles as a multistage delivery system for imaging and therapeutic applications, *Nat. Nanotechnol.* 3 (2008) 151–157.
- [32] J.H. Park, L. Gu, G. von Maltzahn, E. Ruoslahti, S.N. Bhatia, M.J. Sailor, Biodegradable luminescent porous silicon nanoparticles for *in vivo* applications, *Nat. Mater.* 8 (2009) 331–336.
- [33] H. Meng, M. Liong, T. Xia, Z. Li, Z. Ji, J.I. Zink, A.E. Nel, Engineered design of mesoporous silica nanoparticles to deliver doxorubicin and P-glycoprotein siRNA to overcome drug resistance in a cancer cell line, *ACS Nano* 4 (2010) 4539–4550.
- [34] J.S. Ananta, B. Godin, R. Sethi, L. Moriggi, X. Liu, R.E. Serda, R. Krishnamurthy, R. Muthupillai, R.D. Bolskar, L. Helm, M. Ferrari, L.J. Wilson, P. Decuzzi, Geometrical confinement of gadolinium-based contrast agents in nanoporous particles enhances T1 contrast, *Nat. Nanotechnol.* 5 (2010) 815–821.
- [35] T. Tanaka, L.S. Mangala, P.E. Vivas-Mejia, R. Nieves-Alicea, A.P. Mann, E. Mora, H.D. Han, M.M. Shahzad, X. Liu, R. Bhavane, J. Gu, J.R. Fakhoury, C. Chiappini, C. Lu, K. Matsuo, B. Godin, R.L. Stone, A.M. Nick, G. Lopez-Berestein, A.K. Sood, M. Ferrari, Sustained small interfering RNA delivery by mesoporous silicon particles, *Cancer Res.* 70 (2010) 3687–3696.
- [36] C. Chiappini, E. Tasciotti, J.R. Fakhoury, D. Fine, L. Pullan, Y.C. Wang, L. Fu, X. Liu, M. Ferrari, Tailored porous silicon microparticles: fabrication and properties, *ChemPhysChem* 11 (2010) 1029–1035.
- [37] S.Y. Lee, M. Ferrari, P. Decuzzi, Shaping nano-/micro-particles for enhanced vascular interaction in laminar flows, *Nanotechnology* 20 (2009) 495101.
- [38] P. Decuzzi, M. Ferrari, The adhesive strength of non-spherical particles mediated by specific interactions, *Biomaterials* 27 (2006) 5307–5314.
- [39] P. Kim, M. Puoris'haag, D. Cote, C.P. Lin, S.H. Yun, *In vivo* confocal and multiphoton microendoscopy, *J. Biomed. Opt.* 13 (2008) 010501.
- [40] Z. Fan, J. Spencer, Y. Yan Lu, C.M. Pitsillides, G. Singh, P. Kim, S.H. Yun, T.B. Strom, C.P. Lin, M. Koulmanda, *In vivo* tracking of color coded effector, natural and induced regulatory T cells in allograft response, *Nat. Med.* 16 (2010) 718–722.
- [41] K. Kostarelos, A. Bianco, M. Prato, Promises, facts and challenges for carbon nanotubes in imaging and therapeutics, *Nat. Nanotechnol.* 4 (2009) 627–633.
- [42] J.N. Israelachvili, *Intermolecular and Surface Forces, With Applications to Colloidal and Biological Systems*, Second Edition, Academic Press, 1992.
- [43] D.E. Owens III, N.A. Peppas, Opsonization, biodistribution, and pharmacokinetics of polymeric nanoparticles, *Int. J. Pharm.* 307 (2006) 93–102.
- [44] R.E. Serda, E. Blanco, A. Mack, S.J. Stafford, S. Amra, Q. Li, A. van de Ven, T. Tanaka, V.P. Torchilin, J.E. Wiktorowicz, M. Ferrari, Proteomic analysis of serum opsonins impacting biodistribution and cellular association of porous silicon microparticles, *Mol. Imaging* 10 (2011) 43–55.
- [45] D.P. Boso, S.-Y. Lee, M. Ferrari, B.A. Schrefler, P. Decuzzi, Optimizing particle size for targeting the diseased microvasculature: from experiments to artificial neural networks, *Int. J. Nanomedicine* 6 (2011) 1517–1526.
- [46] L.A. van Es, M.R. Daha, Factors influencing the endocytosis of immune complexes, *Adv. Nephrol. Necker Hosp.* 13 (1984) 341–367.
- [47] G. Sharma, D.T. Valenta, Y. Altman, S. Harvey, H. Xie, S. Mitragotri, J.W. Smith, Polymer particle shape independently influences binding and internalization by macrophages, *J. Control. Release.* 147 (2010) 408–412.
- [48] S. Sengupta, D. Eavarone, I. Capila, G.L. Zhao, N. Watson, T. Kiziltepe, et al., Temporal targeting of tumour cells and neovasculature with a nanoscale delivery system, *Nature* 436 (2005) 568–572.
- [49] J.L. West, N.J. Halas, Engineered nanomaterials for biophotonics applications: improving sensing, imaging, and therapeutics, *Annu. Rev. Biomed. Eng.* 5 (2003) 285–292.
- [50] R. Pasqualini, W. Arap, D.M. McDonald, Probing the structural and molecular diversity of tumor vasculature, *Trends Mol. Med.* 8 (2002) 563–571.
- [51] G.Y. Lee, J.H. Kim, G.T. Oh, B.H. Lee, I.C. Kwon, I.S. Kim, Molecular targeting of atherosclerotic plaques by a stabilin-2-specific peptide ligand, *J. Control. Release.* 155 (2011) 211–217.
- [52] J.W. Piper, R.A. Swerlick, C. Zhu, Determining force dependence of two-dimensional receptor–ligand binding affinity by centrifugation, *Biophys. J.* 74 (1998) 492–513.
- [53] C. Pozrikidis, Shear flow over a protuberance on a plane wall, *J. Eng. Math.* 31 (1995) 29–42.